# Microscopic Model for Cyclic Voltammetry of Porous Electrodes

Yiting Lin[ORCID],[1] Cheng Lian[ORCID],[1,*] Mikel Unibaso Berrueta[ORCID],[2] Honglai Liu,[1] and René van Roij[2]

[1]*State Key Laboratory of Chemical Engineering, Shanghai Engineering Research Center of Hierarchical Nanomaterials,*
*School of Chemistry and Molecular Engineering, East China University of Science and Technology, Shanghai 200237, China*
[2]*Institute for Theoretical Physics, Center for Extreme Matter and Emergent Phenomena, Utrecht University,*
*Princetonplein 5, 3584 CC Utrecht, Netherlands*

Cyclic voltammetry (CV) is a widespread experimental technique for characterizing electrochemical devices such as supercapacitors. Despite its wide use, a quantitative relation between CV and microscopic properties of supercapacitors is still lacking. In this Letter, we use both the microscopic "stack-electrode" model and its equivalent circuit for predicting the cyclic voltammetry of electric double-layer formation in porous electrodes. We find that the dimensionless combination $\omega\tau_n$, with $\omega$ the scan frequency of the time-dependent potential and $\tau_n$ the relaxation timescale of the stack-electrode model, governs the CV curves and capacitance: the capacitance is scan-rate independent for $\omega\tau_n \ll 1$ and scan-rate dependent for $\omega\tau_n \gg 1$. With a single fit parameter and all other model parameters dictated by experiments, our model reproduces experimental CV curves over a wide range of $\omega$. Meanwhile, the influence of the pore size distribution on the charging dynamics is investigated to explain the experimental data.

Electric double-layer capacitors (EDLCs) based on carbon electrodes [Fig. 1(a)] have drawn great attention due to their high power density, safety, and extraordinary cycle life [1–8]. Experimental analyses of EDLCs are often based on cyclic voltammetry (CV), which is a powerful technique in which the charge on such electrochemical devices is measured in response to an applied periodic potential [Fig. 1(b)]. CV experiments are widely used to determine the electric properties of supercapacitors as they are (relatively) easy to perform and only require equipment present in almost all electrochemical laboratories [9–16]. Interpreting CV data, however, is not straightforward. On the one hand, the transmission line (TL) circuit model, which was pioneered by De Levie [17] and further developed by Posey and Morozumi [18], can be used to fit the experimental CV curves of EDLCs [17,19–29]. The "standard" TL model treats the porous electrode as circular cylindrical channels, of which the total resistance $R_{tot}$ and capacitance $C_{tot}$ are partitioned over a large number $n$ of branches containing a capacitor of capacitance $2C$ and a resistor of resistance $R'$. However, the number of branches $n$ that is used to fit the CV data by the TL model is typically of order unity, for instance $n = 1$, $n = 5$, and $n = 8$ [19,20,24,25]. Hence, the fitted parameters provide no direct information about the microscopic characteristics of the EDLCs [30]. On the other hand, microscopic models were developed for the time-dependent ionic fluxes and the electric double layer (EDL) formation near idealized electrodes during CV experiments [31]. However, the timescales of the experimental CV measurements are
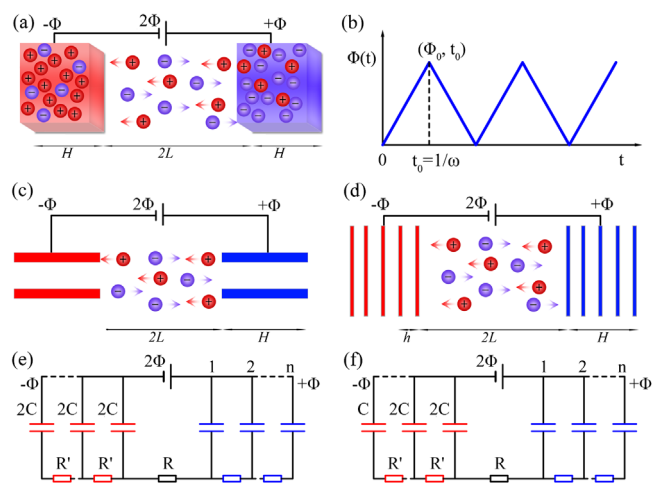


FIG. 1. (a) Sketch of a charged supercapacitor which contains an electrolyte and two porous electrodes of thickness $H$ and a surface-to-surface distance $2L$ connected to a voltage source with a potential difference $2\Phi(t)$. (b) The applied sawtooth potential $\Phi(t)$ that is used in CV experiments and in the present study. (c) Sketch of transmission line model, where the nanoporous cathode (red) and anode (blue) are both modeled by a cylindrical channel of uniform diameter. (d) Sketch of stack-electrode model, where the nanoporous cathode (red) and anode (blue) are both modeled by a stack of $n \geq 1$ parallel planar electrode sheets with a fixed spacing $h$, all subject to the same dimensionless potential $\Phi(t)$ (red) or $-\Phi(t)$ (blue). (e) The equivalent electronic circuit for the transmission line model, where the number of circuit elements $n$ is infinite. (f) The equivalent electronic circuit for the stack-electrode model, where $R \sim L$ and $R' \sim h$.

several orders of magnitude larger than those predicted by microscopic models, which do not account for the multiscale dynamics of electrolytes in porous electrodes.

To remedy these problems, we use the microscopic stack-electrode (SE) model [Fig. 1(d)] [32] to analyze the charging-discharging dynamics of supercapacitors and the influence of the pore size distribution (PSD). Meanwhile, we calculate the analytical result with equivalent circuit called the SE circuit. The SE model simply models two macroscopic electrodes as a "stack" of $n$ planar and permeable electrode sheets of vanishing thickness. In our SE model, $H$ is the thickness of the porous electrodes, $h$ is the average pore size, and $n = H/h + 1$ is the number of the planar and permeable electrodes. These definitions means that the SE parameters in the SE circuit can be inferred from the characteristics of an experimental setup, $R = 2L/(A\epsilon\kappa^2 D)$ and $C = A\epsilon\kappa$. As Figs. 1(e) and 1(f) show, there are small differences between the SE circuit and the TL circuit, which are discussed in the Supplemental Material [33]. Although the results calculated by the SE circuit and the TL circuit are similar, the results calculated by Poisson–Nernst–Planck (PNP) for microscope models are different. Most important of all, the SE model can change the distance between different planar electrodes. Thus, the influence of the PSD can be calculated by the SE model. In short, the SE model has three essential benefits over "standard" TL circuit modeling: the SE model correctly reproduces the biexponential relaxation of porous electrodes [32] (the TL circuit relaxes with a single late-time relaxation time [35]); the SE parameters can be inferred from the characteristics of an experimental setup under consideration; the influence of the PSD and EDL overlap on the charging dynamics of electrolytes can be described by numerically solving the PNP equation of the SE model.

In the SE model analysis, we choose a Cartesian coordinate system with an $x$ axis perpendicular to the electrode stacks and $y$ and $z$ axes in the in plane directions of the electrode sheets. We choose $x = 0$ in the midplane between the two stacks, which are separated by $2L$. Hence, the $i$th microscopic electrodes are located at $\pm X_i = \pm[L + (i-1)h]$, with $i = 1, 2, ..., n$. Notably, the pores in the SE model have a huge lateral extension, $n$ represents the effective number of pores rather than the actual number of pores. In this sense, the index $i = 1, 2, ..., n$ is a proxy for the depth inside the electrode. When the electrode sheets have a large surface area, we can ignore edge effects, and all electrolyte observables only depend on $x$. In particular, we model the local electric potential $(k_B T/e)\phi(x, t)$, the ionic densities $\rho_\pm(x, t)$, and the flux densities $j_\pm(x, t)$ for $|x| \leq L + H$ through the PNP equations [36],

$$\partial_x^2 \phi(x, t) = -\kappa^2 \left[ \frac{z_+ \rho_+(x, t) + z_- \rho_-(x, t)}{z_+^2 \rho_{b,+} + z_-^2 \rho_{b,-}} \right], \quad (1a)$$

$$\partial_t \rho_\pm(x, t) = -\partial_x j_\pm(x, t), \quad (1b)$$

$$j_\pm(x, t) = -D[\partial_x \rho_\pm(x, t) + z_\pm \rho_\pm(x, t)\partial_x \phi(x, t)], \quad (1c)$$

with $k_B$ the Boltzmann's constant, $T$ the temperature, $e$ the elementary charge, and $z_\pm$ the ionic valencies. Moreover, $D$ is the ionic diffusion coefficient, assumed equal among cations and anions, and $\kappa = \sqrt{4\pi\lambda_B(z_+^2 \rho_{b,+} + z_-^2 \rho_{b,-})}$ is the inverse Debye length, where $\rho_{b,\pm}$ are the cationic and anionic bulk number densities and where $\lambda_B = e^2/(4\pi\epsilon k_B T)$ is the Bjerrum length, with $\epsilon$ the electrolyte permittivity. For a $1:1$ electrolyte, $z_+ = -z_- = 1$ and $\rho_{b,\pm} = \rho_b$.

We complement Eq. (1) with three initial and boundary conditions: First, we consider ionic number densities to be uniform initially,

$$\rho_\pm(x, t = 0) = \pm z_\pm \rho_b, \qquad |x| \leq L + H. \quad (2)$$

Second, different from the fully permeable electrodes $i = 1, ..., n - 1$, the outer electrodes are blocking,

$$j_\pm(\pm X_n, t) = 0. \quad (3)$$

Third, to mimic applying a potential difference over the two macroscopic electrodes, we apply a time-dependent dimensionless potential $\Phi(t)$ to all microscopic electrodes,

$$\phi(\pm X_i, t) = \pm \Phi(t). \quad (4)$$

Here, we focus on $\Phi(t)$ of a sawtooth from between zero and a maximum $\Phi_0 > 0$ [cf. Fig. 1(b)], given by

$$\frac{\Phi(t)}{\Phi_0} = \begin{cases} \omega t - 2(u - 1) & 2(u - 1) < \omega t < (2u - 1) \\ 2u - \omega t & (2u - 1) < \omega t < 2u, \end{cases} \quad (5)$$

with $\omega = 1/t_0$ the scan rate, $2t_0$ the oscillation period, and $u = 1, 2, ...$ the cycle number. Focusing on the electrode stack at $x > 0$, we find the unit surface charge density $\sigma_i(t)$ (m$^{-2}$) on the $i$th electrode ($i \neq n$) with Gauss's law, $4\pi\lambda_B \sigma_i(t) = -\partial_x \phi|_{X_i^+} + \partial_x \phi|_{X_i^-}$, with $X_i^-$ and $X_i^+$ the left and right sides of the $i$th electrode. As the $n$th electrode faces the electrolyte only once, its surface charge density reads $4\pi\lambda_B \sigma_n(t) = \partial_x \phi|_{X_n^-}$. In turn, we define the normalized dimensionless electric current density into the $i$th electrode as

$$J_i(t) = \frac{2}{(2n - 1)\bar{\sigma}\omega\Phi_0} \frac{d\sigma_i(t)}{dt}, \quad (6)$$

where $\bar{\sigma} = \kappa/(2\pi\lambda_B)$. Within Gouy-Chapman theory, the unit surface charge density of a single electrode in semi-infinite geometry reads, for small applied potentials, $\sigma = \bar{\sigma}\sinh\Phi/2 = \bar{\sigma}\Phi/2 + O(\Phi^3)$. Hence, during quasi-static charging, $\sigma_i(t) \approx \bar{\sigma}\Phi(t)$ for $i = 1, \ldots, n-1$ and $J_i$ reduces to $J_i = 2/(2n-1)$ [likewise, $J_n = 1/(2n-1)$]. Hence, the prefactor of Eq. (6) causes the total electric current $J = \sum_{i=1}^n J_i$ to sum to $J = 1$ for quasistatic charging. Note that $J$ is proportional to the electric current in the external circuit measured in CV experiments. During discharging, the same expressions hold with minus signs.

Equations (1)–(5) contain seven parameters: $H$, $L$, $h$, and $\kappa$, $D$, $\Phi_0$, and $\omega$. The above parameters can be grouped into many different dimensionless combinations. Here, we will mostly use $H/L$, $\kappa L$, $n$, and $\omega\tau_{\mathrm{RC}}$, with $\tau_{\mathrm{RC}} = L/(\kappa D)$ the relaxation time of RC circuit which has the same geometry $n = 1$ circuit [36,37].
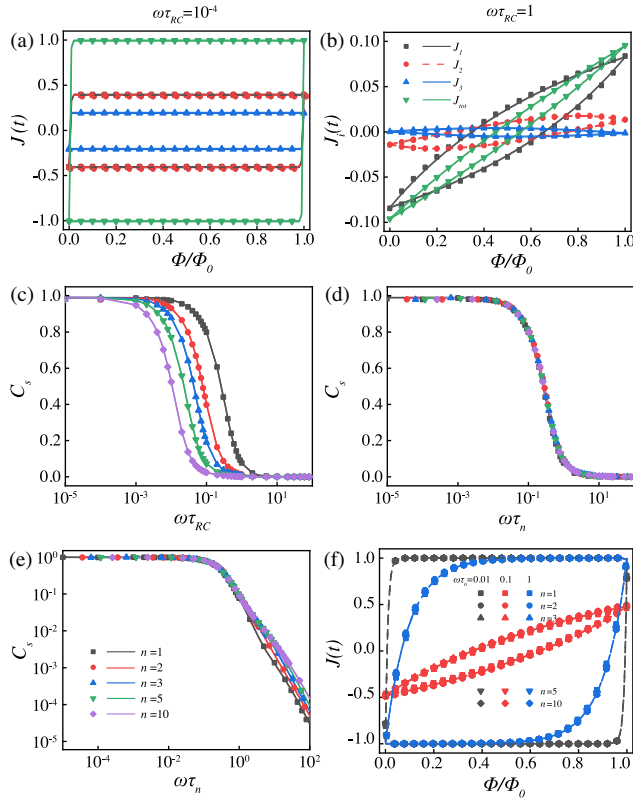


FIG. 2. (a),(b) The cyclic voltammetric curves for $n = 3$, $\kappa L = 100$, $H/L = 1$, and $\Phi_0 = 0.001$, in (a) for low scan rate $\omega\tau_{\mathrm{RC}} = 10^{-4}$, and in (d) for high scan rate $\omega\tau_{\mathrm{RC}} = 1$. The symbols and lines in (a) and (b) correspond to PNP and circuit model calculations. $C_s$ as a function of $\omega\tau_{\mathrm{RC}}$ (c) and as a function of $\omega\tau_n$ (d) and (e), for $\kappa L = 100$, $H/L = 1$, $n = 1, 2, 3, 5, 10$, and $\Phi_0 = 0.001$. Data reflect PNP calculations in the stack-electrode geometry (symbols) and its equivalent circuit (lines). (f) The CV curves for $\kappa L = 100$, $H/L = 1$, $\Phi_0 = 0.001$, different $n = 1, 2, 3, 5, 10$, and $\omega\tau_n = 0.01, 0.1, 1$. In (f) the symbols are calculated by PNP, and the lines are guides to the eye.

Figure 2 compares the results calculated by PNP and equivalent circuit; more details are shown in the Supplemental Material [33]. Clearly, the PNP and equivalent circuit model's predictions agree well. Figures 2(a) and 2(b) present the current vs voltage curves (lines) for two scan rates $\omega\tau_{\mathrm{RC}} = 10^{-4}$ (left) and 1 (right) for a small potential $\Phi_0 = 0.001$ and $\kappa L = 100$, $H/L = 1$, and $n = 3$. At the low scan rate of $\omega\tau_{\mathrm{RC}} = 10^{-4}$, $J_1 = J_2 = 2J_3$, and $J = \pm 1$. The currents are dominated by the quasiequilibrated EDL, which leads for the small applied potential to the scan-rate-independent rectangular CV curves of Fig. 2(a). Conversely, for the large scan rate of $\omega\tau_{\mathrm{RC}} = 1$, the EDLs do not reach quasiequilibrium, and accordingly both the charge adsorbed to the electrode and the current density decrease, leading to scan-rate-dependent lens-shaped CV curves.

We further characterize the CV curves of Figs. 2(a) and 2(b) through the dimensionless areal integral capacitance $C_s$, defined as the area enclosed in a $J - \Phi$ representation during a cycle [38],

$$C_s = \frac{1}{\Phi_0}\oint \frac{J}{2}d\Phi = \frac{1}{\Phi_0}\int_{2(u-1)t_0}^{2ut_0} J\frac{d\Phi}{dt}dt. \quad (7)$$

The notation $C_s$ used here refers to the dimensionless capacitance per surface area as defined in Eqs. (2) and (3) of Ref. [38]. Note the additional factor $1/\omega$ in the integrand of their Eq. (2), which, in our case is absorbed into the definition of $J_i$ in Eq. (6).

Figure 2(c) shows $C_s$ as a function of scan rates $\omega\tau_{\mathrm{RC}}$ for $n = 1, 2, 3, 5, 10$. We observe two $C_s$ regimes for all $n$ considered: $C_s \approx 1$ for $\omega\tau_{\mathrm{RC}} \ll 1$ when EDLs are in quasiequilibrium and $C_s \approx 0$ for $\omega\tau_{\mathrm{RC}} \gg 1$ (see also Ref. [39]). Figure 2(d) presents the same data, but scan rates $\omega$ are now rescaled by the relaxation time $\tau_n$ of the stack-electrode model in response to a step potential [32],

$$\tau_n = \left[\left(2 + 0.75\frac{H}{L}\right)n - 1 - 0.91\frac{H}{L}\right]\tau_{\mathrm{RC}}. \quad (8)$$

With this scaling, data for $C_s$ for the different $n$ collapse onto a single curve. The same $C_s$ data are present in Fig. 2(e) on a log-log scale, which behaves similarly to the maximum current density $J_{\max}$ in the Supplemental Material [33]. Figure 2(f) presents CV curves for different $n$ and fixed $\omega\tau_n$, $\kappa L$, $H/L$, and $\Phi_0$. The collapse of these curves further underlines the importance of the dimensionless combination $\omega\tau_n$ to the CV of the stack electrode model.

In CV experiments with supercapacitors, the scan potential range is often large. Therefore, we now also determine CV curves for applied potentials in the nonlinear screening regime $\Phi_0 \geq 1$. The solid lines in Fig. 3(a) represent CV curves for $\Phi_0 = 0.1, 1, 2$ with $\kappa L = 100$, $H/L = 1$, $n = 5$, and a low scan rate $\omega\tau_{\mathrm{RC}} = 0.01$. The (scaled) CV curves almost overlap at low potentials ($\Phi_0 > 0.1$), but deviate in the nonlinear regime of higher potentials, the more so for
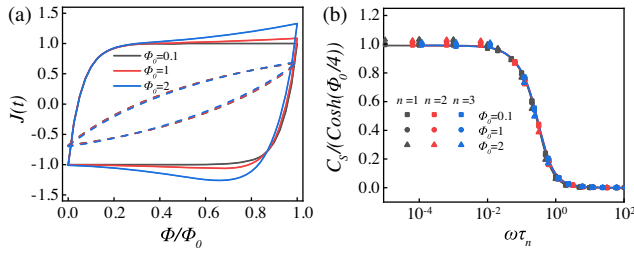
FIG. 3. (a) CV curves for $\kappa L = 100$, $H/L = 1$, $n = 5$, $\Phi_0 = 0.1$, 1, 2, $\omega\tau_{RC} = 0.01$ (solid lines), and $\omega\tau_{RC} = 0.1$ (dashed lines). (b) $\omega\tau_n$ dependence of $C_s/\cosh(\Phi_0/4)$ for $n = 1, 2, 3$ and $\Phi_0 = 0.1, 1, 2$ (symbols). The lines in (b) for different $n$ are calculated with the electronic circuit model.

larger $\Phi_0$. The dashed lines in Fig. 3(a) present the CV curves for the same parameters as the solid lines, except now for $\omega\tau_{RC} = 1$. At this high scan rate, the (scaled) CV curves for different $\Phi_0$ in the linear and the nonlinear screening regime actually all collapse onto the single linear-screening curve.

This scan-rate dependency of the (scaled) CV curves is further illustrated by Fig. 3(b), which shows the capacitance $C_s$ as a function of scaled scan rate $\omega\tau_n$ for $\Phi_0 = 0.1$, 1, 2 and $n = 1, 2, 3$. The scaling of $C_s$ by $\cosh(\Phi_0/4)$ stems from Gouy-Chapman theory, whose static (low-frequency) EDL capacitance reads $C = \epsilon\kappa A\cosh(\Phi/2)$ per surface area $A$, and the average potential during a cycle is $\Phi_0/2$. For all $n$ and $\Phi_0$ considered, the data of Fig. 3(b) collapse onto a single curve. Within the range of validity of our PNP framework, we thus conclude that the CV of our stack-electrode model is fully captured by $\omega\tau_n$, $n$, and $\Phi_0$, at least for the system parameters we considered, the most stringent of which is probably $h \gg \kappa^{-1}$ such that EDLs do not overlap.

To determine the merits of our stack-electrode model, we compare its predictions to the experimental data of Refs. [40]; more details are shown in the Supplemental Material [33]. Reference [40] reports experiments with thickness of electrodes $H = 40$ $\mu$m, surface-to-surface distance $2L = 150$ $\mu$m, average pore size $h = 7.3$ nm, various scan rates $\omega = 0.01$–$5$ s$^{-1}$, and the bulk diffusivity $D = 1.23 \times 10^{-9}$ m$^2$ s$^{-1}$. The maximal applied potential was $\Psi_0 = 0.5$ V, which corresponds to $\Phi_0 \simeq 20$ in our dimensionless units. The electrodes were immersed in 0.5 M Na$_2$SO$_4$ at room temperature, for which $\kappa^{-1} = 0.25$ nm, which is much smaller than the pore size $h$. The SE equivalent electronic circuit is used to fit the experimental data [40] with the sole fit parameter $n$. We find the fitted value $n_1 = 2107$, the fitted average pore size $h_1 = H/(n_1 - 1) = 19$ nm, and the fitted relaxation time $\tau_n = 7.65 \times 10^{-2}$. Notably, the fitted $h_1 = 19$ nm is 2.5 times larger than expected, and the fitted relaxation time $\tau_n = 7.65 \times 10^{-1}$ is 3 orders of magnitude larger than predicted by two plate electrode model $\tau_{RC} = 1.51 \times 10^{-5}$. In Fig. 4, we find good agreement between the SE model
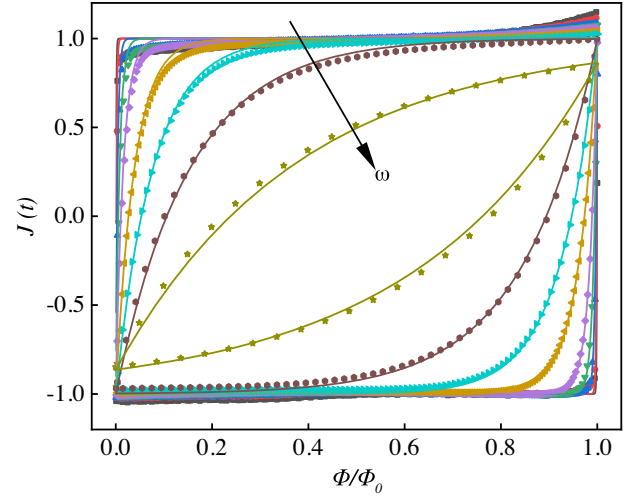


FIG. 4. Comparison of experimental data (symbols) in Ref. [40] and the circuit model (lines) for $\omega = 0.01, 0.02, 0.05, 0.1$, $0.2, 0.5, 1, 2, 5$ s$^{-1}$ corresponding to $0.01$ V s$^{-1}$ to $5$ V s$^{-1}$, with $\Psi_0 = 0.5$ V corresponding to $\Phi_0 \simeq 20$. The direction of the arrow indicates an increase in scanning rate.

(lines) and experiment (dots) with the fit parameter $\tau_n$. However, our oversimplified geometry may cause the overestimate of $n$ previously. The regular microscope SE model considers a uniform spacing $h$ between each successive electrode sheet. However, the PSD function of porous electrodes is often closely approximated by a (continuous) lognormal distribution [41,42]. To discuss the influence of a nontrivial PSD, here, we consider the locations of the $n$ sheets in the stack-electrode model to be set by a (discrete) geometric distribution,

$$\pm X_i = \pm\left[L + \frac{H}{n-1}\frac{n(q^{i-1}-1)}{q^n - 1}\right], \qquad (9)$$

with $q$ the common ratio of the geometric distribution. With this choice, the spacing of the electrodes becomes narrower toward $x = \pm(L + H)$. Repeating our numerical CV
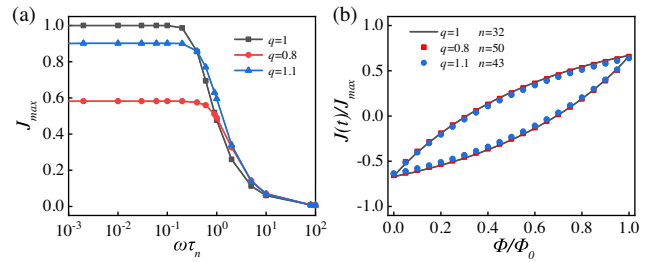


FIG. 5. (a) Predicted $J_{\max}$ as a function of $\omega\tau_n$ for $\Phi_0 = 0.001$, $\kappa L = 1000$, $H/L = 1$, $n = 50$, and $q = 1, 0.8$, and $1.1$. (b) $J(t)/J_{\max}$ vs $\Phi/\Phi_0$ for $\Phi_0 = 0.001$, $\kappa L = 1000$, $H/L = 1$, $q = 1, 0.8, 1.1$, and $\omega\tau_{RC} = 7.375 \times 10^{-3}$. Here, we determined $J_{\max}$ at $\omega\tau_n = 10^{-3}$ from the data in panel (a). Conversely, $J(t)$ and $\Phi(t)$ for the different $n$ were evaluated at $\omega\tau_{RC} = 7.375 \times 10^{-3}$. This treatment ensures that all the scaled currents in (b) vary between $-1$ and 1, similar to Fig. S8 [33].

experiments for this amended stack-electrode model, we first determine $J_{max}$ for $\Phi_0 = 0.001$, $\kappa L = 1000$, $H/L = 1$, $n = 50$, and $q = 0.8$, 1, 1.1. Figure 5(a) shows that $J_{max} < 1$ if $q \neq 1$. Next, Fig. 5(b) shows $J(t)/J_{max}$ vs $\Phi/\Phi_0$ for $\omega\tau_{RC} = 7.375 \times 10^{-3}$, $q = 1$, $n = 32$ (black line), and other parameters as in Fig. 5(a). For $q = 0.8$ and $q = 1.1$ (symbols) we tune $n$ such that their CV curves coincide with the data for $q = 1$. Both for $q$ smaller and larger than 1, one needs a larger $n$ to accomplish such overlap. This suggests that the larger-than-expected fitted $h_1 = 19$ nm (smaller-than-expected fitted $n_1 = 2107$ by approximately 80–50%) may be (partially) caused by our neglect of nontrivial PSD in the regular SE model [Note that the scale factor $J_{max}$ in Fig. 5(b) was determined from the data in Fig. 5(a) at $\omega\tau_n = 10^{-3}$. This treatment ensures that all the scaled currents in (b) vary between $-1$ and 1.]. To predict the effective pore size even better, further models could include effects of finite ion sizes, concentration-dependent diffusivity, intricate pore network structure, etc.

In summary, we calculate CV curves of electrolyte-immersed porous electrodes through the stack-electrode model. It is comforting that the good agreement of the equivalent electronic circuit to model the response to a stepwise potential [32] is now found to be extendable to the response to the sawtooth potential for cyclic voltammetry. Contrary to the circuit models often used to fit experimental CV curves, the (number of) capacitors and resistors in our circuit model are one-to-one related to the parameters of the stack-electrode model. We identify the dimensionless combination $\omega\tau_n$ to be the key parameter that governs the CV curves of the stack-electrode model with $n$ and relaxation time $\tau_n$ [Eq. (8)]. Our model can reproduce recent experimental data over a large range of scan rates and be used to estimate the pore size of an electrode. However, a quantitative connection to experimental measurements of the pore size, such as Brunauer Emmett Teller test, is beyond the SE model and requires a better account of the 3D structure of an actual porous electrode.

Y. L. and C. L. contributed equally to this work.

---

*liancheng@ecust.edu.cn

[1] J. Chmiola, G. Yushin, Y. Gogotsi, C. Portet, P. Simon, and P.-L. Taberna, Science **313**, 1760 (2006).

[2] A. C. Forse, J. M. Griffin, C. Merlet, J. Carretero-Gonzalez, A.-R. O. Raji, N. M. Trease, and C. P. Grey, Nat. Energy **2**, 16216 (2017).

[3] C. Prehal, C. Koczwara, H. Amenitsch, V. Presser, and O. Paris, Nat. Commun. **9**, 4145 (2018).

[4] D. T. Limmer, C. Merlet, M. Salanne, D. Chandler, P. A. Madden, R. van Roij, and B. Rotenberg, Phys. Rev. Lett. **111**, 106102 (2013).

[5] P. Simon and Y. Gogotsi, Acc. Chem. Res. **46**, 1094 (2013).

[6] T. Mouterde, A. Keerthi, A. Poggioli, S. Dar, A. Siria, A. Geim, L. Bocquet, and B. Radha, Nature (London) **567**, 87 (2019).

[7] C. Cheng, G. Jiang, C. J. Garvey, Y. Wang, G. P. Simon, J. Z. Liu, and D. Li, Sci. Adv. **2**, e1501272 (2016).

[8] K. Namink, X. Meng, M. T. M. Koper, P. Kukura, and S. Faez, Phys. Rev. Applied **13**, 044065 (2020).

[9] R. G. Compton and C. E. Banks, *Understanding Voltammetry*, 2nd ed. (Imperial College Press, Singapore, 2010).

[10] E. Barsoukov and J. R. Macdonald, *Impedance Spectroscopy Theory, Experiment, and Applications* (John Wiley & Sons, New York, 2005).

[11] Y. Gogotsi and R. M. Penner, ACS Nano **12**, 2081 (2018).

[12] S. Bi, M. Chen, R. Wang, J. Feng, M. Dinca, A. A. Kornyshev, and G. Feng, Nat. Mater. **19**, 552 (2020).

[13] Z. Li, S. Gadipelli, H. Li, C. A. Howard, D. J. Brett, P. R. Shearing, Z. Guo, I. P. Parkin, and F. Li, Nat. Energy **5**, 160 (2020).

[14] S. Aderyani, P. Flouda, S. Shah, M. Green, J. Lutkenhaus, and H. Ardebili, Electrochim. Acta **390**, 138822 (2021).

[15] D. Kim, C. Zhou, M. Zhang, and M. Cargnello, Proc. Natl. Acad. Sci. U.S.A. **118**, e2113382118 (2021).

[16] Z. Liang, T. Wu, T. Ye, M. Tangming, R. Qiao, and G. Feng, Nat. Comput. Sci. **1**, 725 (2021).

[17] R. de Levie, Electrochim. Acta **8**, 751 (1963).

[18] F. A. Posey and T. Morozumi, J. Electrochem. Soc. **113**, 176 (1966).

[19] M. W. Verbrugge and P. Liu, J. Electrochem. Soc. **153**, A1237 (2006).

[20] W. Pell and B. Conway, J. Electroanal. Chem. **500**, 121 (2001).

[21] F. Fabregat-Santiago, I. Mora-Ser, G. Garcia-Belmonte, and J. Bisquert, J. Phys. Chem. B **107**, 758 (2003).

[22] W. G. Pell and B. E. Conway, J. Power Sources **96**, 57 (2001).

[23] M. Mirzadeh, F. Gibou, and T. M. Squires, Phys. Rev. Lett. **113**, 097701 (2014).

[24] T. Kulova and A. Skundin, Russ. Chem. Bull. **69**, 1672 (2020).

[25] J. E. Stark, A. Allison, and H. Andreas, Carbon **170**, 245 (2020).

[26] M. Metiko-Hukovi and S. Omanovi, J. Electroanal. Chem. **455**, 181 (1998).

[27] J. P. Zheng, Electrochem. Solid-State Lett. **2**, 359 (1999).

[28] E. G. Gagnon, J. Electrochem. Soc. **122**, 521 (1975).

[29] T. Wang, R. L. Sacci, J. Liang, C.-L. Do-Thanh, J. Fan, H. Chen, Y. Sun, B. P. Thapaliya, S. M. Mahurin, M. Zhou, J. Wu, S. W. Donne, and S. Dai, J. Electrochem. Soc. **168**, 060530 (2021).

[30] J. F. Rubinson and Y. P. Kayinamura, Chem. Soc. Rev. **38**, 3339 (2009).

[31] H. Wang and L. Pilon, Electrochim. Acta **64**, 130 (2012).

[32] C. Lian, M. Janssen, H. Liu, and R. van Roij, Phys. Rev. Lett. **124**, 076001 (2020).

[33] See Supplemental Material at http://link.aps.org/supplemental/10.1103/PhysRevLett.128.206001 for details of our equivalent circuit model calculations, for additional PNP data for other parameters, for Fig. 5 redrawn with separate panels for each $\omega$, and for a discussion of the relationship between stack electrode model and transmission line model, which includes Ref. [35].

[34] J. Hale, *Theory of Functional Differential Equations* (Springer, New York, NY, 1977).

[35] M. Janssen, Phys. Rev. Lett. **126**, 136002 (2021).

[36] M. Z. Bazant, K. Thornton, and A. Ajdari, Phys. Rev. E **70**, 021506 (2004).

[37] M. Janssen and M. Bier, Phys. Rev. E **97**, 052616 (2018).

[38] H. Wang and L. Pilon, Electrochim. Acta **64**, 130 (2012).

[39] H. Wang, A. Thiele, and L. Pilon, J. Phys. Chem. C **117**, 18286 (2013).

[40] Y. Bu, H. Liang, R. Shi, H. Liu, Y. Zhang, T. Sun, C. Lian, X. Shen, and H. Li, ACS Sustainable Chem. Eng. **8**, 12430 (2020).

[41] X. Wang, A. Y. Mehandzhiyski, B. Arstad, K. L. Van Aken, T. S. Mathis, A. Gallegos, Z. Tian, D. Ren, E. Sheridan, B. A. Grimes, D.-e. Jiang, J. Wu, Y. Gogotsi, and D. Chen, J. Am. Chem. Soc. **139**, 18681 (2017).

[42] Y. Gogotsi and P. Simon, Science **334**, 917 (2011).